One-pot Synthesis of the MIL-100 (Fe) MOF/MOX Homojunctions with Tunable Hierarchical Pores for the Photocatalytic Removal of BTXS

Lu Chen [a,b], Xiao Wang [b,*], Zepeng Rao [b], Zixia Tang [b], Gansheng Shi [b], Yan Wang [b], Guanhong Lu [b], Xiaofeng Xie [b], Deliang Chen [a,c,**], Jing Sun [b,*]

[a] School of Materials Science and Engineering, Zhengzhou University, Zhengzhou 450001, China
[b] State Key Lab of High Performance Ceramics and Superfine Microstructure, Shanghai Institute of Ceramics, Chinese Academy of Sciences, 585 Heshuo Road, Shanghai 201899, China
[c] School of Materials Science and Engineering, Dongguan University of Technology, Dongguan 523808, China

ARTICLE INFO

ABSTRACT

The construction of metal-organic frameworks (MOFs) with hierarchical pores is of great importance for the photocatalytic oxidation (PCO) of gaseous BTXS (benzene, toluene, xylenes and styrene) pollutants with large molecular size, but it is still challenging. Herein, by adjusting the ratio of anions (NO_3^- and Cl^-) in the metal precursors, hierarchically porous MIL-100(Fe) MOF/MOX homojunctions were obtained through a one-pot solvothermal method. The existence of both micro- and mesopores (2–10 nm) made the active sites more accessible to guest molecules. The formation of MOF/MOX homojunctions promoted the separation of electron-hole pairs. Additionally, the coordinatively unsaturated acidic Fe_3-O sites facilitated the capture of BTXS molecules and participated in the PCO process through the conversion between Fe(III) and Fe(II). The MIL-100(Fe) homojunctions showed improved performance towards the PCO of BTXS (over 80% for xylenes and styrene) compared with the crystalline or xerogel counterparts and exhibited great potential in the PCO of aromatic air pollutants.

1. Introduction

As more and more attention has been paid to the problem of air pollution, the removal of BTXS (the main component of VOCs) becomes very urgent [1–3]. The photocatalytic oxidation (PCO) is regarded as an effective way for the removal of BTXS due to its low cost and easy accessibility [4]. Metal-organic frameworks (MOFs) represent a series of crystalline porous material built from metal ions (or metal clusters) and organic ligands [5–7]. As a newly arising material with large specific surface area and tunable pore structure, MOFs have drawn widespread interests in gas storage/separation, molecular sensing, drug carriers and catalysis [7–11]. Among a variety of MOFs, Fe-MOFs including MIL-100 (Fe), MIL-88B(Fe) et al. have shown great potential in the photocatalytic elimination of BTXS due to their suitable bandgap and high affinity towards aromatic species [12,13]. One important requirement of these applications is the fast and massively absorption of target molecules. However, though exhibiting high specific surface area, most MOFs reported today show micropores with an average diameter less than 2 nm,

which are not favorable for the migration of guest molecules to the active sites [14,15]. Besides, some MOFs like MIL-100, MIL-101 et al., have cage-like pore structures [16], which may further limit the fully interaction of guest molecules with the catalysts and hinder the photocatalytic reaction to a certain extent. Hence, pore structure regulation is the key to further improving the ability of MOFs in catalyzing gas-phase reaction.

Direct synthesis and post treatment are the two methods commonly used in regulating the pore structure of MOFs [17]. In a direct synthesis process, researchers modify the pore size of MOFs by adjusting the species of organic ligands. However, the modification of ligands may significantly affect the stability and intrinsic properties of MOFs [18]. In a post treatment procedure, partially corrosion of MOFs is generally used to create new pores or cavities inside the MOFs nanoparticles. Although the intrinsic properties of the MOFs can be retained, the effect of this method is strongly restricted by the hydrophilicity, corrosion resistance of MOFs, and the post treatment parameters, which severely limits its application [19].

---

* Corresponding authors.
** Corresponding author at: School of Materials Science and Engineering, Zhengzhou University, Zhengzhou 450001, China.
E-mail addresses: wangxiao@mail.sic.ac.cn (X. Wang), dlchen@zzu.edu.cn (D. Chen), jingsun@mail.sic.ac.cn (J. Sun).

The MOF Gel state (MOG) has attracted prominent attention recently. As reported in previous works, unlike crystalline MOFs, MOGs are composed of discrete crystalline nanoparticles combined by weak non-covalent Van der Waals interactions [20,21]. By removing the solvent from MOGs, the MOFs xerogels (noted as MOXs) can be obtained, which were proven to have both micro- and mesopores. Due to the existence of these mesopores, MOXs expose more active sites and allow the free migration of large molecules, which make them promising material in practical application [22]. However, due to the incomplete growth of MOFs crystals, intrinsic deficiencies also come alone. The insufficient crystallization of MOXs not only results in a decrease in the amount of micropores and a smaller specific surface area compared with crystalline MOFs, but also leads to the fast recombination of photo-induced charge carriers. Besides, the reasonable design of pores inside the MOXs still remains a challenge.

Based on the analysis above, we propose a homojunction material which can combine both the hierarchical pore-structure of MOXs and the high photocatalytic activity of crystalline MOFs. By adjusting the initial crystallization rate, MOF/MOX (metal-organic framework /metal-organic xerogel) homojunctions based MIL-100(Fe) with both hierarchical pores and improved PCO activity were synthesized. Iron nitrate nonahydrate ($Fe(NO_3)\cdot 9H_2O$) and Ferric chloride hexahydrate ($FeCl_3\cdot 6H_2O$) were selected to coordinate with trimesic acid (H_3BTC, organic ligands) to construct the MIL-100(Fe) MOF/MOX homojunctions. The MIL-100(Fe) xerogel was obtained with $Fe(NO_3)\cdot 9H_2O$ alone as the Fe precursor and the crystalline MIL-100(Fe) synthesized with $FeCl_3\cdot 6H_2O$ was also fabricated as the contrasts. The MIL-100(Fe) MOF/MOX homojunctions were found to be efficient in the PCO of BTXS with the removal efficiency of 83.1% for o-xylene, 23% for benzene, 41% for toluene, 82% for p-xylene, 79% for m-xylene and 83% for styrene. The reaction rate constant for o-xylene was up to 0.00267 min^{-1}, which was 1.30 times and 1.73 times higher than of MOXA-1 and MOXA-5.

2. Experiments

2.1. Materials

Iron nitrate nonahydrate ($Fe(NO_3)\cdot 9H_2O$), Ferric chloride hexahydrate ($FeCl_3\cdot 6H_2O$), N, N-dimethylformamide (DMF) and trimesic acid (H_3BTC) were purchased from Shanghai adamas Reagent Co., Ltd. Anhydrous ethanol was produced from Sinopharm Chemical Reagent Co., Ltd. Deionized water for experiment was prepared by ultrapure water machine (Tondino Scientific (Shanghai) Co., Ltd). The organic solvents, including DMF and anhydrous ethanol, were not further purified before being used in the experiment.

2.2. The synthesis of the MIL-100(Fe) MOF/MOX homojunctions

The MIL-100(Fe) MOF/MOX homojunctions were prepared by a classical coordination reaction between metal sources ($Fe(NO_3)_3\cdot 9H_2O$ and $FeCl_3\cdot 6H_2O$) and trimesic acid (H_3BTC) through the solvothermal method. The amount of metal sources ($Fe(NO_3)_3\cdot 9H_2O$: $FeCl_3\cdot 6H_2O$ = 0.75:0.25, 0.5:0.5, 0.25:0.75) and organic ligands (H_3BTC) was controlled at 1 mmol, respectively. After dissolving the metal sources and H_3BTC in DMF solution under magnetic stirring, the solution was transferred to a 100 mL polytetrafluoroethylene liner. The liner was then placed in a stainless steel and aged at 150 °C for 16 h in the oven. The product was washed with DMF and ethanol in turn for three times, respectively. The DMF inside was then fully replaced with ethanol. The MIL-100(Fe) MOF/MOX homojunctions obtained after vacuum drying were donated as 0.75 NO_3^--0.25 Cl^--BTC (MOXA-2), 0.50 NO_3^--0.50 Cl^--BTC (MOXA-3) and 0.25 NO_3^--0.75 Cl^--BTC (MOXA-4), respectively. The MIL-100(Fe) xerogel (noted as MOXA-1) and crystalline MIL-100(Fe) particles (noted as MOXA-5) were also prepared as the above preparation method except that a single metal source was used ($Fe(NO_3)_3\cdot 9H_2O$

and $FeCl_3\cdot 6H_2O$ corresponding to MOXA-1 and MOXA-5, respectively).

2.3. Characterization

Power X-ray diffraction (PXRD, Bruker D8 advanced diffractometer with Cu- Kα) was used to characterize the phase composition of the as-prepared samples over a 2 theta degree = 3–50° at scan rate of 2°/min. The structure information of MOXA samples was recorded with Raman spectrum (DXR, ThermoFisher Scientific) and a Fourier Transform Infrared spectrometer (Vertex 70, ThermoFisher Scientific) in the range of 4000–400 cm^{-1}. The specific surface area of the MOXA samples was researched by nitrogen adsorption-desorption test through BET Surface Area Analyzer (Quadrasorb SI). The X-ray photoelectron spectroscopy (XPS, ESCAlab250 in USA) was used to analyze the oxidation states of Fe in the MOXA samples and the chemical environment of surface. Field emission scanning electron (Magellan 400, USA) and transmission electron microscope (JEM-2100F, Japan) were used to study the morphology and microstructure of MOXA samples. The light adsorption behaviors of the different MOXA samples were investigated by UV-Vis diffuse reflectance spectra (DRS, Cary 5000 in USA). Photoluminescence spectroscopy (LS55 spectromete, Perkin Elmer Instruments) was used to study the electronic structure information of the MOXA samples with the excitation wavelength at 320 nm. A photoelectrochemical workplace (chi650b, CH Instrument Company, Shanghai) equipped with a three-electrode system was used to characterize the transient photocurrent of the samples. The trapping of active radicals was carried on a electron spin resonance spectrometer (ESR, JES-FA200). The adsorption properties of the as-prepared samples for gaseous BTXS were studied by a VOCs-Temperature-programmed desorption (TPD) instrument (ChemiSorb PCA-1200, Bibuilder, China). The surface acidity of the MOXA samples was also measured by the TPD with NH_3 as probe molecules. The concentrations of BTXS in the process of adsorption and photocatalytic degradation were measured by gas chromatography (GC-7920, Beijing China Education Au-light Co., Ltd., China) with a flame ionization detector (FID) detector, and the concentration of CO_2 was detected by GC-FID equipped with a nickel catalyst accessory for converting low-level CO_2 to methane. The intermediates of the photocatalytic degradation of BTXS were detected by *in-situ* Diffuse Reflection Infrared Fourier Transform spectroscopy (DRIFTS, Shimadzu IRTracer-100).

2.4. Characterization of the adsorption and photocatalysis performance of the MOXA samples

A gas reaction device for flow phase was used to investigate the adsorption and photocatalysis activity of the MOXA samples to BTXS at ambient temperature as shown in Scheme S1. This device contained the gas mixing system, the photocatalytic reaction chamber and the detection system. In the gas mixing system, the compressed air generated by a nitrogen-hydrogen-air integrated generator passed through a humidifier and brought water into the reaction chamber to adjust the environmental humidity. The relative humidity (RH) was controlled at 60% to simulate the atmospheric environment by adjusting the flow rate of air and the amount of water in the humidify tank. The flow rates of air and BTXS were both set at 10 sccm by gas flowmeters. Before flowing into the reaction chamber, the compressed air and standard BTXS gas were mixed in the gas mixing tank and the concentration of o-xylene molecules was set at 25 ppm. A glass slide (12 × 5 cm) coated with the MOXA photocatalyst (0.05 g) was placed in the photocatalytic reaction chamber (15 × 8 × 1 cm) after drying at 60 °C for 1 h and a 250 W Xenon lamp as the light irradiation source was suspended 30 cm above the photocatalytic reaction chamber. A GC was used to monitor the real-time concentration of BTXS during the adsorption and photocatalysis processes. The saturated adsorption capacity (A, μmol/g) of BTXS was calculated by the following expression:

$$A = \frac{c_0 \times \rho_0 \times \rho_1 \times \left\{ \left(\int_0^t \upsilon \times c \, dt \right)_{blank} - \left(\int_0^t \upsilon \times c \, dt \right)_{sample} \right\}}{M \times m} \quad (1)$$

where c_0 (ppm) and c were the initial concentration of BTXS and the real-time concentration of BTXS recorded at regular intervals, respectively. ρ_0 (g/cm^3) and ρ_1 represented air density and relative vapor density of gaseous o-xylene at room temperature. t (min) was time point of data recording and υ (mL/min) was the current velocity of the mixed gas. M (g/mol) and m (g) were molar mass and mass of BTXS, respectively. The removal ratio (η) of BTXS was enumerated according to Eq. (2).

$$\eta = (1 - C/C_0) * 100\% \quad (2)$$

3. Results & Discussion

3.1. Composition and hierarchically porous characteristics of the MIL-100(Fe) MOF/MOX homojunctions

The X-ray diffraction (XRD) patterns of the MOXA samples were displayed in Fig. 1a, which agreed well with the simulated XRD pattern of single crystalline MIL-100(Fe) [23,24], demonstrating that the MOXA samples have similar crystalline structure as the bulk MIL-100(Fe). The peak at $2\theta = 3$–$5°$ gradually shifted to small angles with the amount of NO_3^- increased, indicating an increase in the lattice spacing. In order to further understanding the structure of the MIL-100(Fe) MOF/MOX homojunctions and the coordination of metal centers, the element composition and chemical state of the MOXA was subsequentially carried out by XPS (Fig. S1). The deconvolution of the Fe 2p spectra for MOXA-1, MOXA-2 and MOXA-5 were shown in Fig. 1b. Only the peak

for Fe(III) (711.8 eV) was found in MOXA-5, which was in consistence with the XPS spectra of crystalline MIL-100(Fe) reported previously [25, 26]. Interestingly, peaks assigned to Fe(II) (710.3 eV) and Fe(III) (711.8 eV) were both observed in MOXA-1 and MOXA-2, revealing the existance of unsaturated coordinated Fe sites in these samples. Similar results were obtained in the FTIR analysis (Fig. S2). Compared with the band at 621 cm^{-1}, which was assigned to the Fe_3-O groups of MOXA-5 (Fig. 1c), an obvious peak shift from 621 cm^{-1} to 615 cm^{-1} was observed in MOXA-2 and MOXA-1, further confirming the existence of Fe(II) [27,28]. Raman spectroscopy was employed to probe the difference between the samples in the molecular structure level (Fig. 1d). Peaks were observed at 805, 1225 cm^{-1} (deformation vibration of C-H in benzene ring), 1537 cm^{-1} (asymmetric stretching vibrations of C-O$_2$), 1465 cm^{-1} (symmetric vibrations of C–O$_2$) and 1605 cm^{-1} (stretching vibrations of C=C) in MOXA-5, in accordance with Raman spectra of crystalline MIL-100 (Fe) reported previously [29,30]. However, the peak at 1225 cm^{-1} shifted to 1201 cm^{-1} and two strong peaks at 1132 cm^{-1} (in-plane blending of C-H) and 1507 cm^{-1} (stretching vibrations of C=C of benzene ring) appeared in MOXA-1 [31], which indicated that differences existed in the MIL-100(Fe) xerogel and crystalline particles caused by different anions in molecular structure level, resulting in the divergence in optical absorbance [32].

Fig. 2 gives the SEM images of the MOXA samples and the EDS of MOXA-2. MOXA-1 showed a typical morphology of MIL-100(Fe) xerogel with a flat surface and small pores, while nanoparticles with an average diameter of 25 nm were observed in MOXA-5. By gradually replacing NO_3^- with Cl$^-$, a network structure with small nanoparticles dispersing on three dimensional skeletons (Fig. 2c, d, e, f, g, and h) were obtained in the MOXA-2, MOXA-3, and MOXA-4. A close connect was formed between MIL-100(Fe) xerogel and newly formed crystalline MIL-100(Fe) particles, indicating the formation of MIL-100(Fe) MOF/MOX
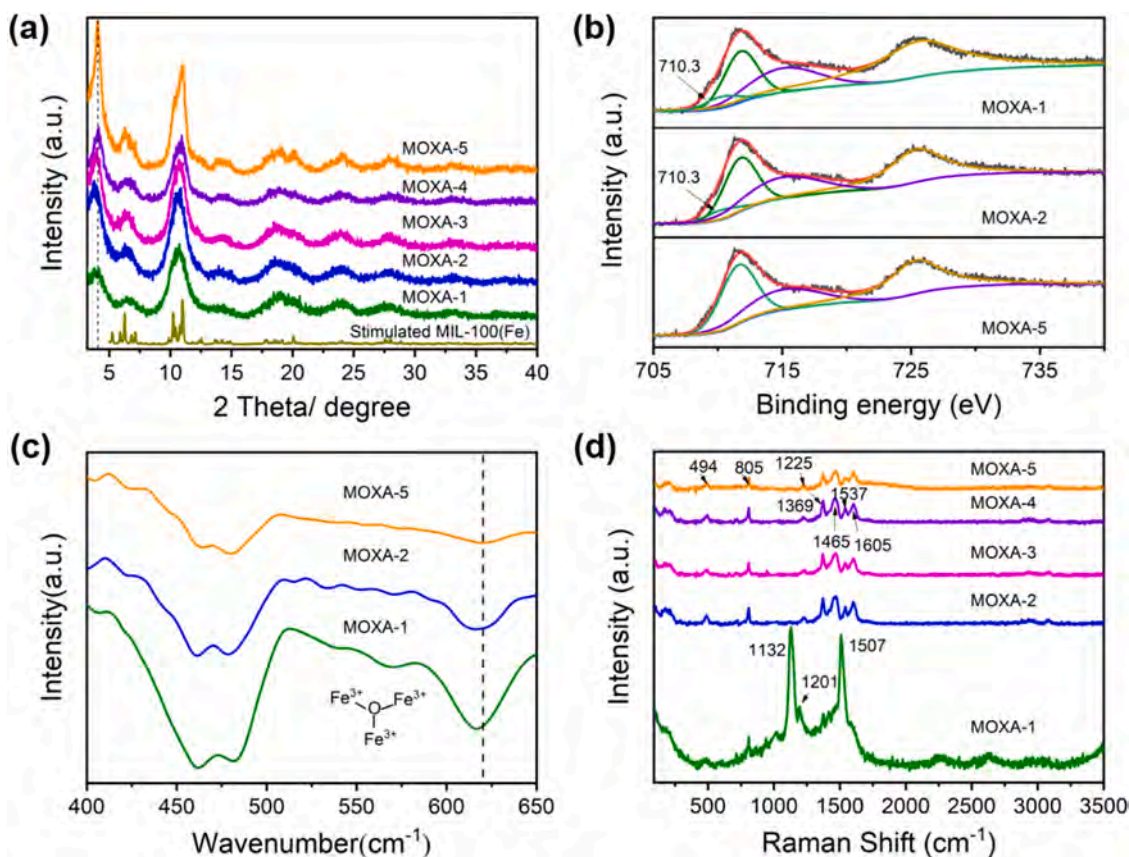

Fig. 1. (a) XRD patterns of MOXA-1, MOXA-2, MOXA-3, MOXA-4, MOXA-5 and stimulated MIL-100(Fe) (b) The deconvolution of XPS spectrum of Fe 2p in MOXA-1, MOXA-2 and MOXA-5 (c) FTIR spectrum of MOXA-1, MOXA-2 and MOXA-5 (d) Raman spectrum of MOXA-1, MOXA-2, MOXA-3, MOXA-4 and MOXA-5.
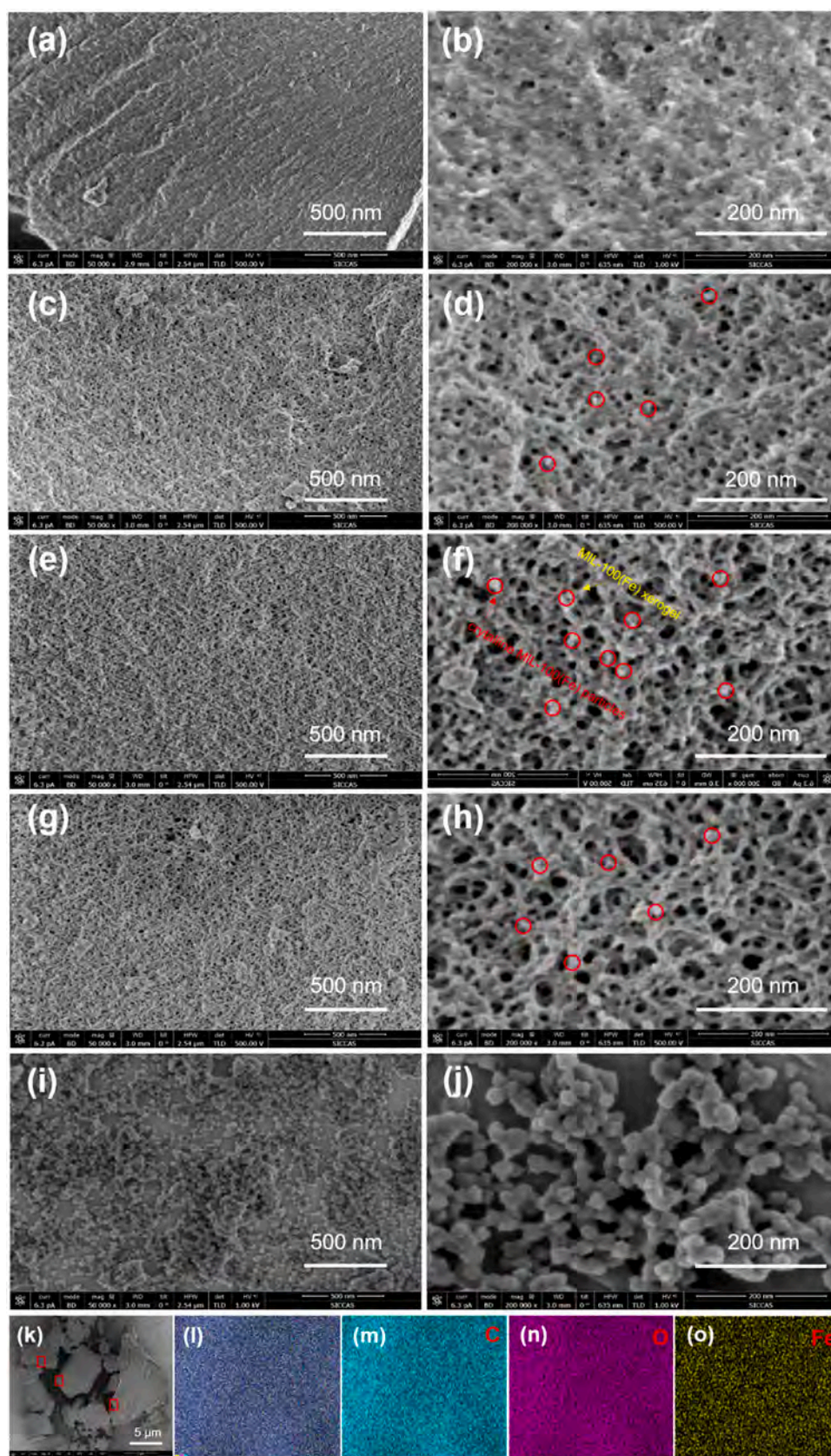
Fig. 2. SEM images of (a) and (b) for MOXA-1, (c) and (d) for MOXA-2, (e) and (f) for MOXA-3, (g) and (h) for MOXA-4, (i) and (j) for MOXA-5, (k–o) energy dispersive X-ray spectroscopy (EDX) mappings of C, O and Fe elements of MOXA-2.

homojunctions. A large amount of channels was observed inside the network, and the channel structure became more and more obvious with the increase of heterogeneity (Fig. 2 and Fig. S3). The element mapping results demonstrated that Fe, C and O were uniformly distributed in MOXA-2 (Fig. 2k–o) and the content of each element was shown in Fig. S4 and Table S1.

In the purpose of further understanding the micro-structure of the MIL-100(Fe) MOF/MOX homojunctions, BET analysis was used to research the N_2 isotherms and the pore size distribution of the samples (Fig. 3 and Table S2). All the MOXA samples showed type I adsorption curves with a sharp rise in the low P/P_0 region, indicating the existance of abundant micropores (Fig. 3a) [22,33]. Unlike the circumstance of MOXA-5, which gave a type II curve in the high P/P_0 region, type IV curves characterized by the H2-type hysteresis loops were observed in the MOXA 1–4 samples, which represented the existence of meso-/-macropores [14]. Similar result was obtained in the pore size distribution of the samples (Fig. 3b). MOXA-5 presented the highest concentration of micropores with diameters smaller than 2 nm, while pores larger than 3 nm were detected in MOXA-1 and MIL-100(Fe) MOF/MOX homojunctions (MOXA-2, MOXA-3 and MOXA-4). Interestingly, the concentration of both micro- and mesopores were higher in the composites compared with MOXA-1. The crytalline MOFs particles in the composites could not only ensure the generation of more micropores, but also turn the microstructure of MOXA 1–4 into a network with larger pores ranging from 6.7, 8.8, 9.7, to 10.2 nm, which enabled the formation of hirechical pores. In addition to the hirechical pores, the MIL-100(Fe) MOF/MOX homojunctions also showed high specific surface areas comparable to MOXA-5, which was conducive to both the adsorption and diffusion of gas-phase macromolecular pollutants.

3.2. The synthesis mechanism of the MIL-100(Fe) MOF/MOX homojunctions

Based on the above discussion, the formation mechanism of the MIL-100(Fe) MOF/MOX homojunctions was proposed, which involved multiple stages (Scheme 1). Interestingly, unlike the yellow color of the solution of $FeCl_3·6H_2O$, a red solution was obtained by dissolving Fe $(NO_3)_3·9H_2O$ into DMF, indicating the dissociation of $Fe(NO_3)_3$ and the coordination of Fe(III) with DMF (Fig. S5) [34]. After the addition of H_3BTC, the color of the solution gradually turned into red-brown, which might be caused by the slowly deprotonation of H_3BTC and the replacement of DMF by BTC^{3-}. Unlike the circumstance of Fe $(NO_3)_3·9H_2O$, almost no color change was observed when using $FeCl_3·6H_2O$ as the Fe precursor, which could be related to the slow or even no dissociation of $FeCl_3$ in DMF. When starting the solvothermal reaction, the Fe-complex formed during the initial stage started to grow into small MOF nuclei and an explosive nucleation happened, which consumed most of the Fe precursors and impeded the following growth of the nuclei into nanoparticles. As the viscosity of the reaction system increased, these nuclei would assemble through Van Der Waals interaction to form a MOFs gel instead of precipitations (Fig. S6). The removing of DMF solvent through centrifugation finally turned the gel into MIL-100(Fe) xerogel. On the contrary, the slow dissociation of $FeCl_3$ enabled a limited nucleation process and the nuclei would slowly grow into crystalline MOFs nanoparticles. In the case where $Fe(NO_3)_3·9H_2O$ and $FeCl_3·9H_2O$ were applied, both of the above processes occurred. Fe (III) in $Fe(NO_3)_3·9H_2O$ would coordinate with BTC^{3-} until it was completely consumed during the initial stage of the synthesis and then form nuclei during the solvothermal reaction. Fe(III) in $FeCl_3·6H_2O$ was then attracted by the carboxyl groups of unsaturated coordinated BTC^{3-} through electrostatic interaction and reacted with them to facilitate the growth of part of the formed MOFs nuclei into crystalline nanoparticles. With the self-assembly process of small crystals into MIL-100(Fe) gel, the crystalline nanoparticles were embedded in the gel. After removing the solvent from the gel, the MIL-100(Fe) MOF/MOX homojunctions with a 3-D network structure dispersed by with small nanoparticles was obtained. As illustrated by Figs. S6 and S7, the MIL-100(Fe) gel gradually transferred into precipitations as the proportion of $FeCl_3·9H_2O$
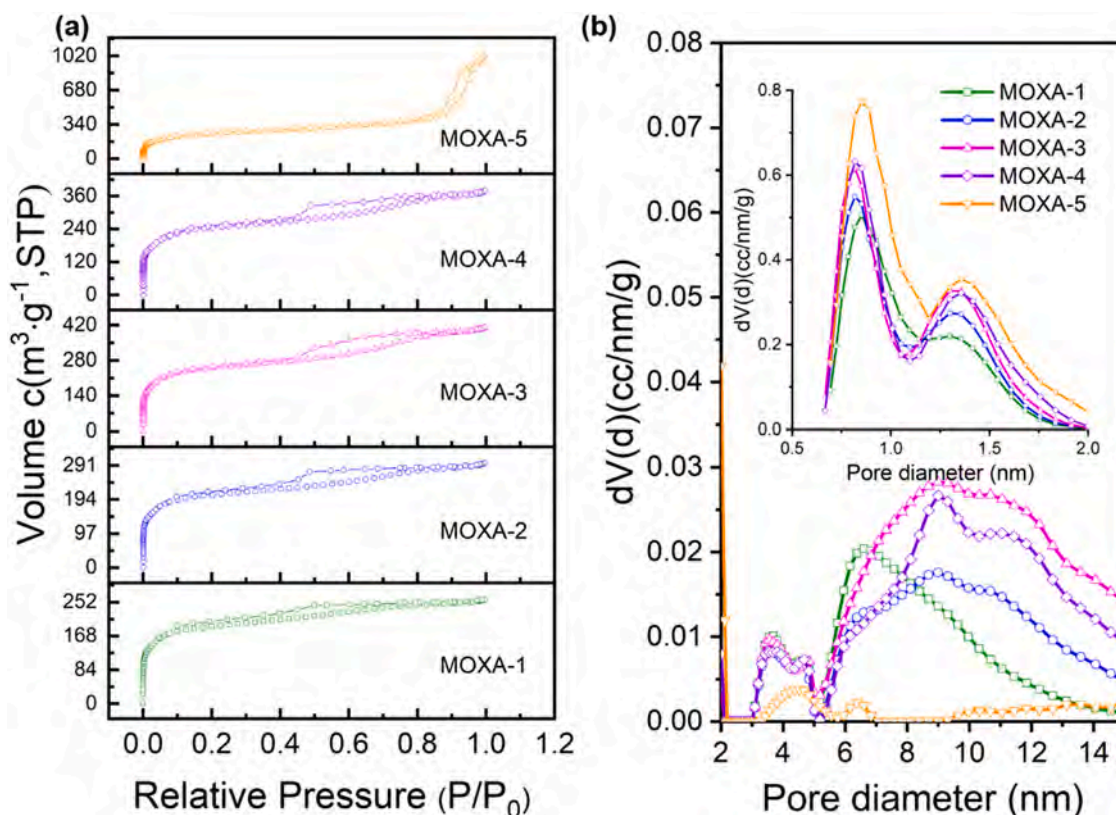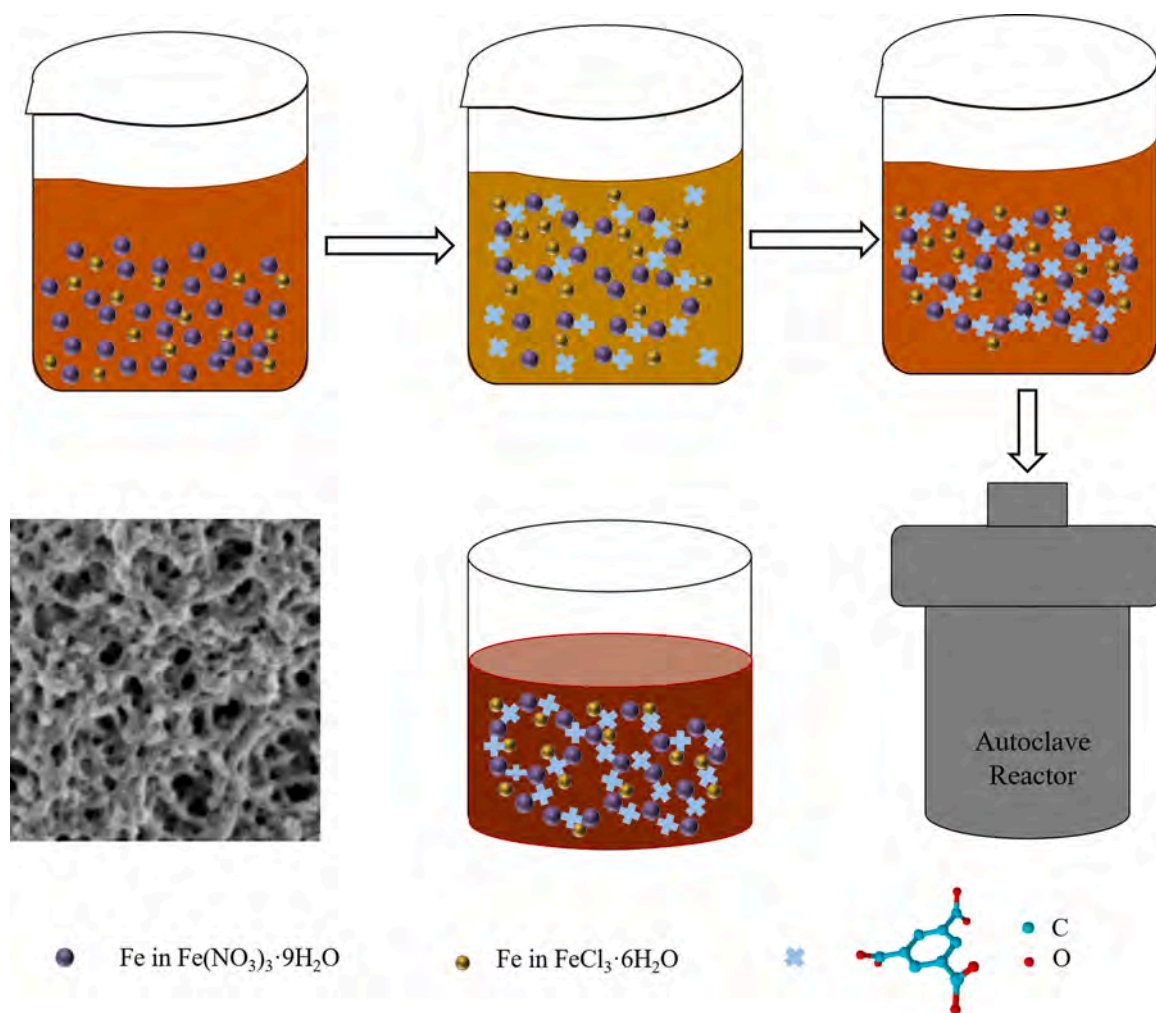

Fig. 3. (a) N_2 adsorption-desorption isotherms and (b) pore size distributions of MOXA-1, MOXA-2, MOXA-3, MOXA-4 and MOXA-5.

Scheme 1. Schematic diagram of the MIL-100(Fe) MOF/MOX homojunctions formation mechanism.

increased, which further confirmed our proposal. This result confirmed for the first time that the dissociation rate of metal ions could be controlled by adjusting the anion species, so as to control the structure and morphology of MOFs.

3.3. Adsorption performance and mechanism of the photocatalysts towards BTXS

In order to verify the potential of the as-prepared MIL-100(Fe) MOF/ MOX homojunctions in the PCO of BTXS pollutants, o-xylene was chosen as the target pollutant and the PCO reactions were carried out in a reaction system as shown by Scheme S1. The adsorption of target molecules by the catalyst is the prerequisite for high-efficiency photocatalysis. Therefore, an adsorption-desorption equilibrium was firstly achieved before starting the light irradiation to study the adsorption capacity of MOXA samples towards o-xylene. As shown by Fig. 4a, compared with the blank chamber, the concentration of o-xylene was much lower when the catalysts were applied, proving the effective adsorption of o-xylene molecules. All of the as-prepared samples showed substantial adsorption capacity towards gaseous o-xylene (as calculated by Eq. (1)) (Fig. 4b) [12,35]. Interestingly, although MOXA-5 showed the largest specific surface area, its adsorption capacity for o-xylene molecules was not the highest, which might be attributed that the micropore structure and small pore size of MOXA-5 hindered the diffusion of o-xylene molecules in the channels of the photocatalyst. Benefiting from the exposure of more active sites and the smooth diffusion of o-xylene molecules inside the mesoporous pores, MOXA-2

achieved a high absorption capacity to o-xylene (18.1 μmol/g) comparable to the MOXA-3 (17.8 μmol/g), MOXA-4 (19.6 μmol/g) and MOXA-5 (18.5 μmol/g). In addition, the adsorption behavior of gaseous o-xylene on the MOXA samples were further studied by Temperature-Programmed Desorption (TPD). Two peaks centered at around 105 $^\circ$C and 223 $^\circ$C were observed for MOXA-5 (Fig. 4c). As reported by Zhang et al., [36] the first peak could be assigned to the weak adsorption by the micropores, while the peak at 223 $^\circ$C was attributed to both the adsorption by Fe$_3$-O with acidity and the π-π interaction between guest o-xylene molecules and the ligand of MOXA-5. The intensity of the peak at 105 $^\circ$C decreased significantly in MOXA-2 and MOXA-1, which was in accordance with relative smaller concentration of micropores inside these samples. The temperature of the desorption peak of MOXA-2 (232 $^\circ$C) was higher than that of MOXA-1 (222 $^\circ$C) and MOXA-5 (223 $^\circ$C), implying a stronger binding force between o-xylene molecules and MOXA-2 [37]. In order to further clarify the roles of Fe$_3$-O acidic sites and π-π interaction in the adsorption of o-xylene, the surface acidity of the catalysts was explored by NH$_3$-TPD (Fig. 4d) [38]. The peak areas for MOXA-1, MOXA-2 and MOXA-5 were calculated as 270.0, 261.4 and 235.6, respectively, meaning that the content of acidic sites in MOXA-2 was higher than in MOXA-5, but slightly lower than in MOXA-1. Interestingly, the amount of o-xylene absorbed by both MOXA-5 and MOXA-2 was larger than by MOXA-1. Therefore, the π-π interaction might take up a larger proportion in the adsorption of o-xylene by MOXA-5, while the adsorption of o-xylene by Fe$_3$-O acidic sites plays a more important part in the MOXA-1. The difference might originate from the pore structure of these samples. As reported by
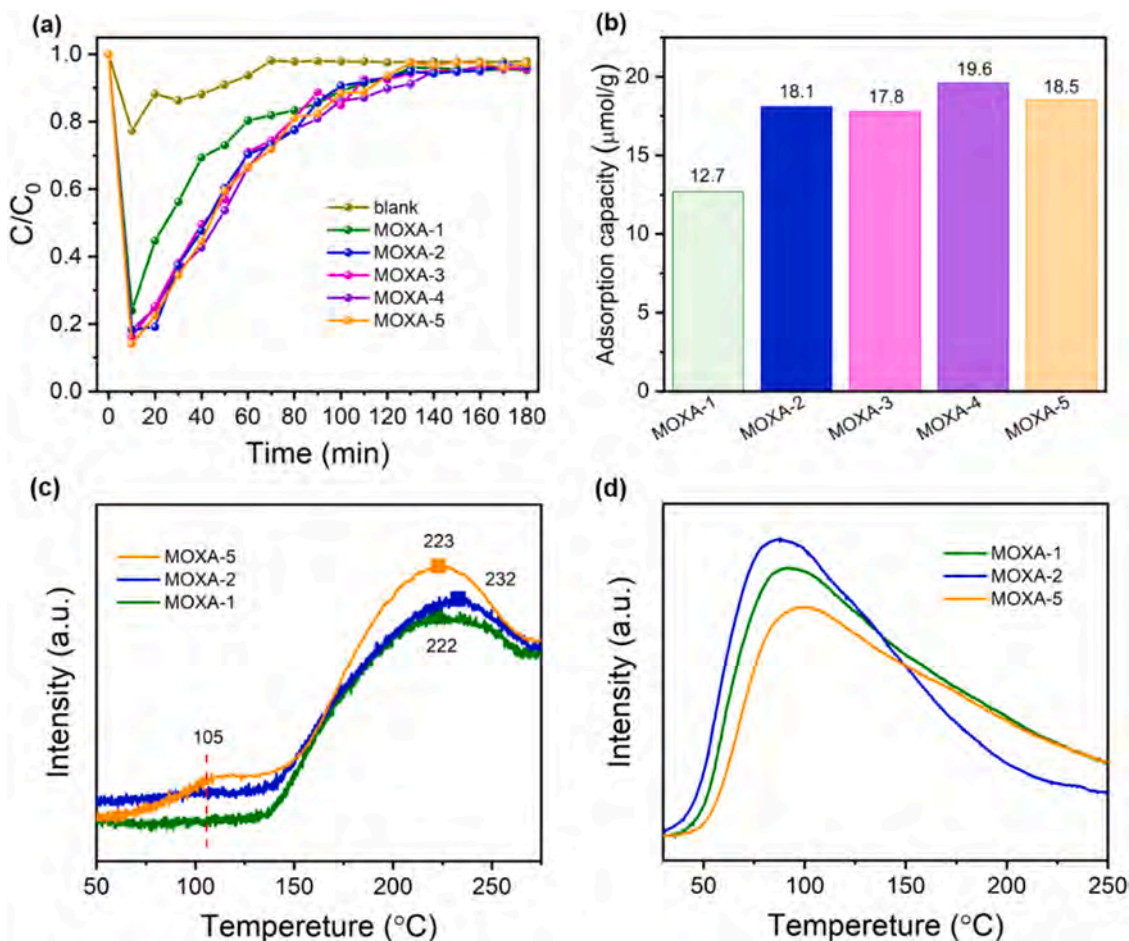
Fig. 4. (a) Adsorption curves of flowing gaseous o-xylene molecules for different samples in dark condition, (b) The saturated adsorption capacity of 50 mg as-prepared materials for gaseous o-xylene (25 ppm), Temperature-programmed desorption (TPD) (c) for gaseous o-xylene and (d) for gaseous NH_3 of MOXA-1, MOXA-2 and MOXA-5.

Khajavi et al., [39] during the adsorption of BTXS by MOFs, the guest molecules would preferentially fill up the micropores and forming π-π interaction with the ligand. Compared with MOXA-5, the incomplete crystallization of MOX resulted in a decrease in the amount of micropores in MOXA-1 and MOXA-2. However, the coordinatively unsaturated Fe sites in these two samples provided abundant open sites for the adsorption of o-xylene. Benefiting from the hierarchical pores and abundant acidic sites, the MIL-100(Fe) MOF/MOX homojunctions showed great potential in the photocatalytic removal of BTXS pollutants.

3.4. The adsorption and utilization of incident light of the photocatalysts

In addition to the adsorption of BTXS, the ability of the photocatalysts in utilizing incident light and generating oxidative radicals are also decisive factors in determining their photocatalytic performance. A red-shift was observed in the light-absorption curve of MOXA-1 compared with the other samples (Fig. 5a) in accordance with Raman spectrum. By combining the converted Tauc plots *versus* photon energy (*hν*) according to the UV-Vis diffuse reflectance spectra and the HOMO
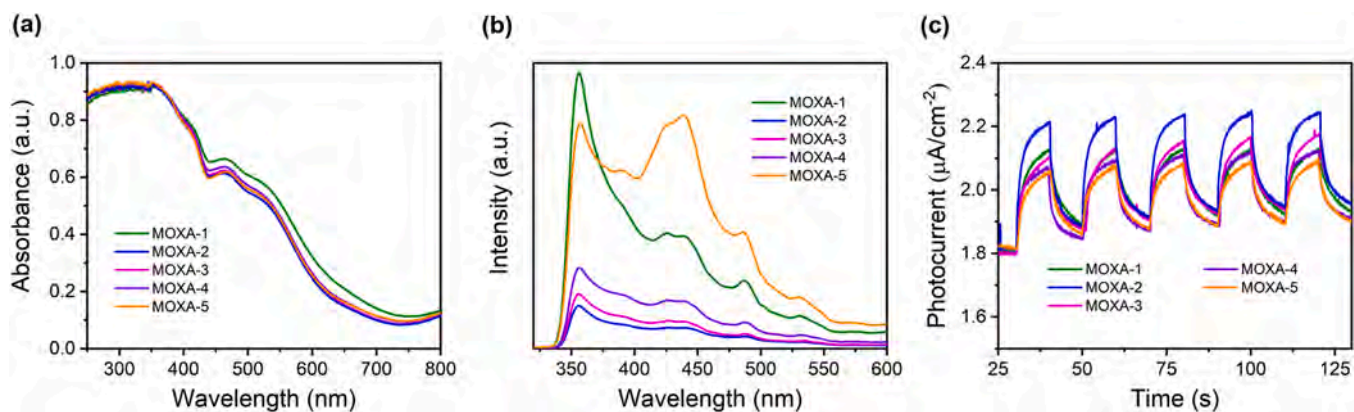

Fig. 5. (a) Diffuse reflectance spectroscopy (b) Photoluminescence spectroscopy and (c) Photocurrent response of MOXA-1, MOXA-2, MOXA-3, MOXA-4, and MOXA-5.

(highest occupied molecular orbital) energy level based on XPS analysis (Fig. S8), MOXA-1 was calculated to have a HOMO energy level slightly more positive than MOXA-5 and a more positive LUMO (lowest unoccupied molecular orbital) energy level than MOXA-5. As a consequence, a built-in electric field [40] formed at the interface between the two phases when constructing the MIL-100(Fe) MOF/MOX homojunctions (MOXA-2, MOXA-3 and MOXA-4). The formation of homojunctions could be further confirmed by the PL results given by Fig. 5b. Compared with crystallined MIL-100(Fe) (MOXA-5) and MIL-100(Fe) xerogel (MOXA-1), much weaker PL intensities were observed in the MIL-100 (Fe) MOF/MOX homojunctions. As PL intensity represents the re-combination rate of electron-hole pairs generated under light irradiation, the reduced PL intensities confirmed that the electron-hole recombination was effectively suppressed in the homojunctions. Similar trend were obtained in the photocurrent tests, with MOXA-2 showing the highest photocurrent intensity (Fig. 5c). Based on the results above, the generation and migration of charge carriers in the homojunctions could be proposed. Electrons generated in the crystalline MIL-100(Fe) particles could spontaneously diffuse to the skeleton formed by MIL-100(Fe) xerogel while the holes would migrate reversely, resulting in an electron-depletion layer at the side of particles and an electron accumulation layer at the side of xerogel. As the Fermi energies tended to be consistent at the interface region, the Fermi level of MOXA-1 turned upward while the Fermi level of MOXA-5 moved downward (Scheme 2). The band bending at the interface resulted in the recombination of electrons in the LUMO of MOXA-1 and holes in the HOMO of MOXA-5 under the Coulombic attraction [41,42], leaving the photogenerated electrons and the holes conserved in the LUMO of MOXA-5 in the HOMO of MOXA-1, which then participated in the photocatalytic degradation of BTXS.

3.5. Photocatalytic performance of the photocatalysts to BTXS

After reaching the adsorption-desorption equilibrium in dark, a 250 W Xenon light was employed as the light source to test the performance of the MOXA samples in the photocatalytic degradation of o-xylene. The photocatalytic removal efficiency of o-xylene by the as-prepared MOXA samples calculated by Eq. (2) was displayed in Fig. 6a. Thanks to the exposure of abundant Fe_3-O active sites, the removal efficiency of o-xylene by MOXA-1 (69.7%) was slightly higher than that of MOXA-5 (63.4%). However, the removal efficiency of MOXA-1 gradually decreased and tended to lose its photocatalytic activity in 60 min, while MOXA-5 maintained its original photocatalytic

activity. Compared with the typical MIL-100(Fe) xerogel (MOXA-1) and crytalline MIL-100(Fe) (MOXA-5), the MIL-100(Fe) MOF/MOX homojunctions (MOXA-2, MOXA-3 and MOXA-4) showed both improved photocatalytic removal efficiency (83.1%, 80.6% and 79.4%) and high stability in 150 min, and this was higher than that of commercial TiO_2 for o-xylene (13%) under the same test conditions (Fig. S9). Based on the above results, kinetics of photocatalytic degradation depended on time was evaluated by the pesudo-first-order kinetic model (Eq. (S1)) [37, 43]. The k (apparent first-order reaction rate constant, min^{-1}) values were calculated as 0.00205 min^{-1}, 0.00267 min^{-1}, 0.00234 min^{-1}, 0.00219 min^{-1}, and 0.00154 min^{-1} for MOXA-1, MOXA-2 MOXA-3 MOXA-4, and MOXA-5, respectively (Fig. 6b). MOXA-2 exhibited the highest reaction rate, which was 1.30 times and 1.73 times than that of MOXA-1 and MOXA-5, respectively. The possible reasons for the excellent performance of the MIL-100(Fe) MOF/MOX homojunctions were summarized as follows: (1) The large specific surface area and hierarchical pores of the MIL-100(Fe) MOF/MOX homojunctions reduced the diffusion resistance of gaseous o-xylene and enabled the effective contact between o-xylene molecules and the active sites for PCO reactions. (2) The formation of homojunction between MIL-100(Fe) xerogel and crystals promoted the spatial separation of charge carriers and therefore accelerated the generation of active radicals for the oxidation of o-xylene. Cyclic experiments were carried out to study the stability and durability of the MOXA-2 in the PCO elimination of o-xylene (Fig. S10a). After 4 cycles, the photocatalytic degradation efficiency of MOXA-2 remained at 82% and no obvious change was observed in the intrinsic structure of the photocatalyst (Fig. S10b). Two new peaks assigned to the vibration of C-OH (1195 cm^{-1}) of phenol and the vibration of C=C (2024 cm^{-1}) appeared in the FTIR spectra of MOXA-2 after the cyclic reactions, which might be attributed to the absorbed intermediates generated during the PCO of o-xylene [44,45].

To prove the universal applicability MIL-100(Fe) MOF/MOX homojunctions in the photocatalytic removal of BTXS, the performance of MOXA-2 in the PCO of benzene, toluene, p-xylene, m-xylene and styrene was detected and the corresponding efficiencies were calculated as 23%, 41%, 82%, 79% and 83%, respectively (Fig. S11 a, b, e, d, and e). The high stability and universality made the as-prepared MIL-100(Fe) MOF/ MOX homojunctions promising photocatalysts for the in-door air purification.
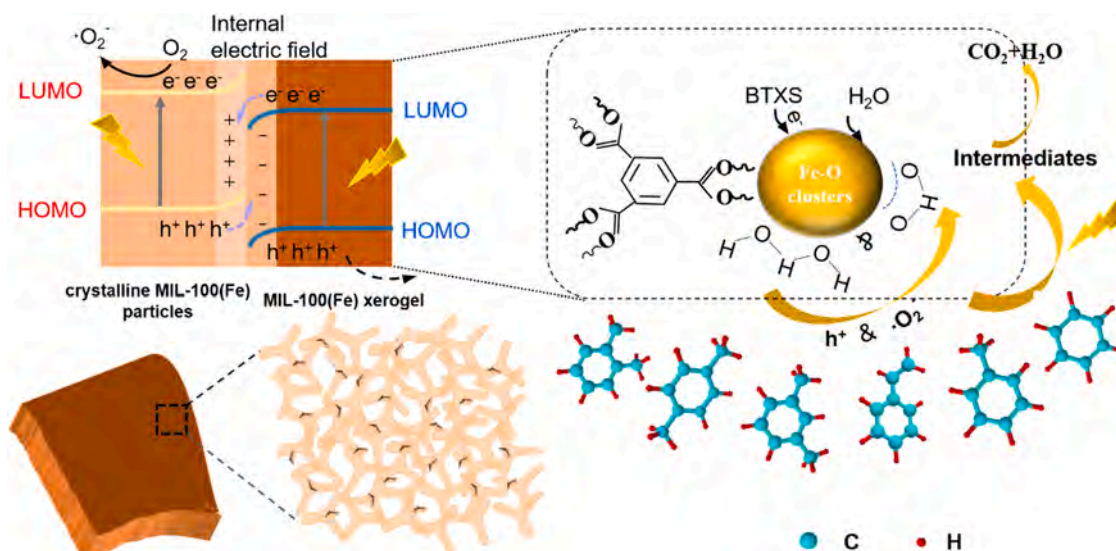
Scheme 2. The mechanism of photocatalytic degradation of BTXS on the MIL-100(Fe) MOF/MOX homojunctions.
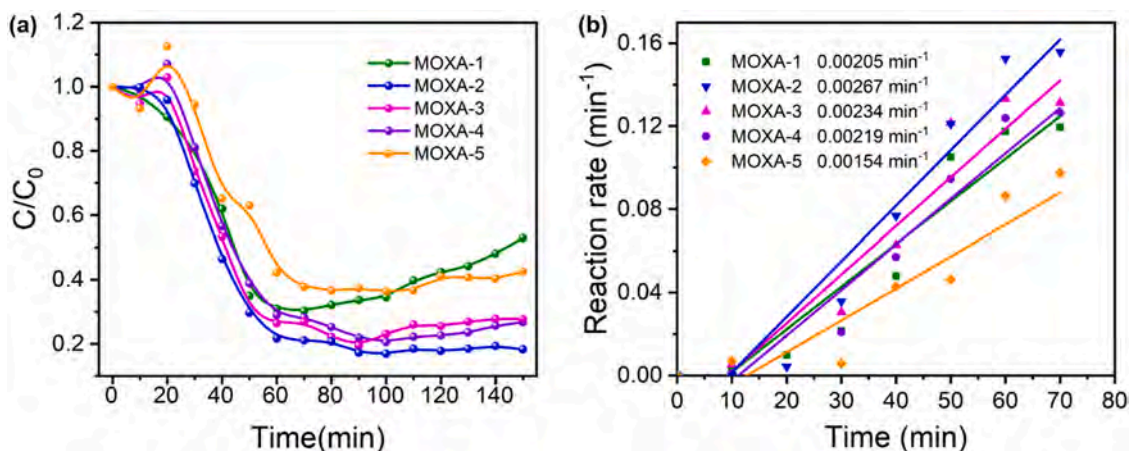
Fig. 6. (a) The photocatalytic removal efficiency of gaseous o-xylene under a 250 W Xenon irradiation and (b) corresponding pesudo-first-order kinetic model for as-prepared MOXA samples.

3.6. The mechanism of photocatalytic degradation of BTXS on the MIL-100(Fe) MOF/MOX homojunctions

In order to further explore the degradation mechanism of BTXS, the variation in the concentration of Fe(III) in MOXA-2 and the generation of oxidative radicals were analyzed by a electron spin resonance spectrometer (ESR). As shown in Fig. 7a, the concentration of Fe(III) firstly decreased during the absorption of o-xylene and then increased after starting the light illumination, which indicated that Fe(III) was consumed in the process of adsorption and then supplemented under light illumination [46,47]. Due to the relatively lower energy of holes, the oxidation of H_2O into ·OH radicals did not happen in all the samples and only ·O_2^- were detected (Fig. 7b and Fig. S12). In accordance with the PL and photocurrent results, MOXA-2 gave the highest amount of ·O_2^- radicals, much higher compared with the MOXA-5. Interestingly, though exhibiting higher PL intensity and lower photocurrent intensity, the amount of ·O_2^- radicals generated by MOXA-1 was similar to MOXA-2. As reported by Bloch et al., [48] the high density of Fe_3-O acidic sites detected in MOXA-1 promoted the adsorption and activation of O_2, which might be the main reason for the generation of large amount of ·O_2^- radicals in MOXA-1. In addition, a significant increase in the absorption capacity of MOXA-2 for o-xylene increased from 18.1 μmol/g to 74.1 μmol/g and the removal efficiency of MOXA-2 for o-xylene decreased from 83.1% to 51.6% when the RH reduced from 60% to 45%. (Fig. S13). Hence, although no hydroxyl radical was not observed in the ESR results (Fig. S12), water molecules might interact with Fe_3-O clusters to form catalytic active sites similar to Fe_3-O(OH) to degrade o-xylene into CO_2 and H_2O [49].

The *in-situ* DRIFTS was also applied to monitor the intermediates on the MOXA-2 to investigate the mechanism of photocatalytic degradation of BTXS. The reaction was performed in a mixture of o-xylene and air whose flow rates were controlled at 10 sccm, in accordance with the experimental conditions for obtaining kinetic data. The background of MOXA-2 in *in-situ* DRIFTS was deducted before the adsorption and degradation of o-xylene began. As shown in Fig. 8, the bands at 1450–1650 cm^{-1} (the skeleton vibration of C=C in benzene ring), 2335, 2368 cm^{-1} (antisymmetric stretching vibration of C=O in CO_2), 3605 cm^{-1} (the stretching vibration of O-H), and 3740 cm^{-1} (free water) were observed during the process of dark adsorption, indicating that o-xylene, CO_2 and H_2O molecules were adsorbed on the surface of MOXA-2 [50]. After the adsorption equilibrium was reached, the data of photocatalytic degradation towards o-xylene was subsequently recorded by the *in-situ* DRIFTS with the Xenon light on. The peaks at 1100 cm^{-1} and 1222, 1745 cm^{-1} appeared, corresponding to the vibration of C-OH in aliphatic alcohols and the vibration of C=O in aromatic aldehyde, respectively, which were mainly due to the oxidation of o-xylene by ·O_2^- radicals [51–53]. The peak at 2050 cm^{-1} (the vibration of cumulative C=C) was detected, attributing to the opening of benzene ring in
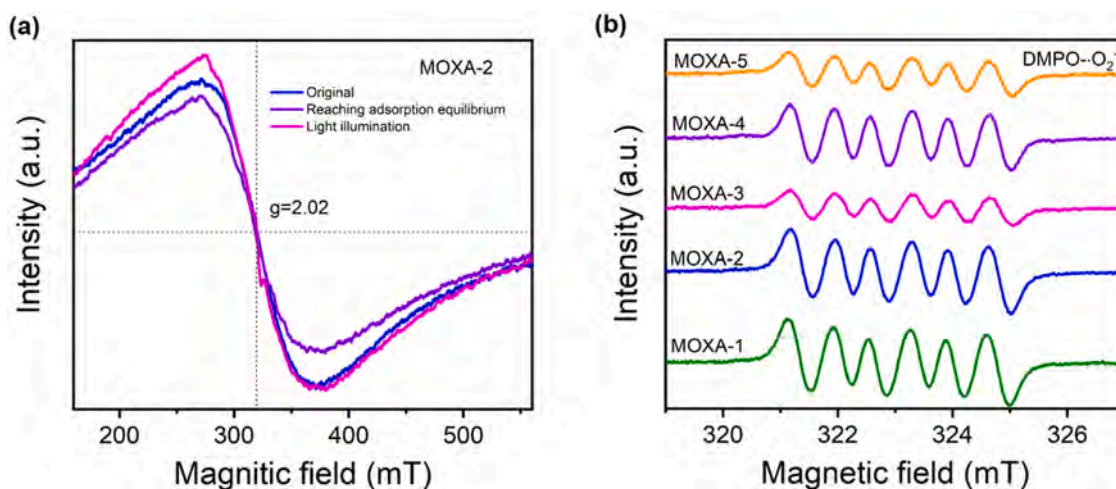

Fig. 7. (a) The Fe(III) signals of ESR spectra of MOXA-2 reaching adsorption equilibrium in the dark and after light irradiation (b) DMPO spin-trapping ESR spectra for the ·O_2^- of as-prepared samples in ethanol.
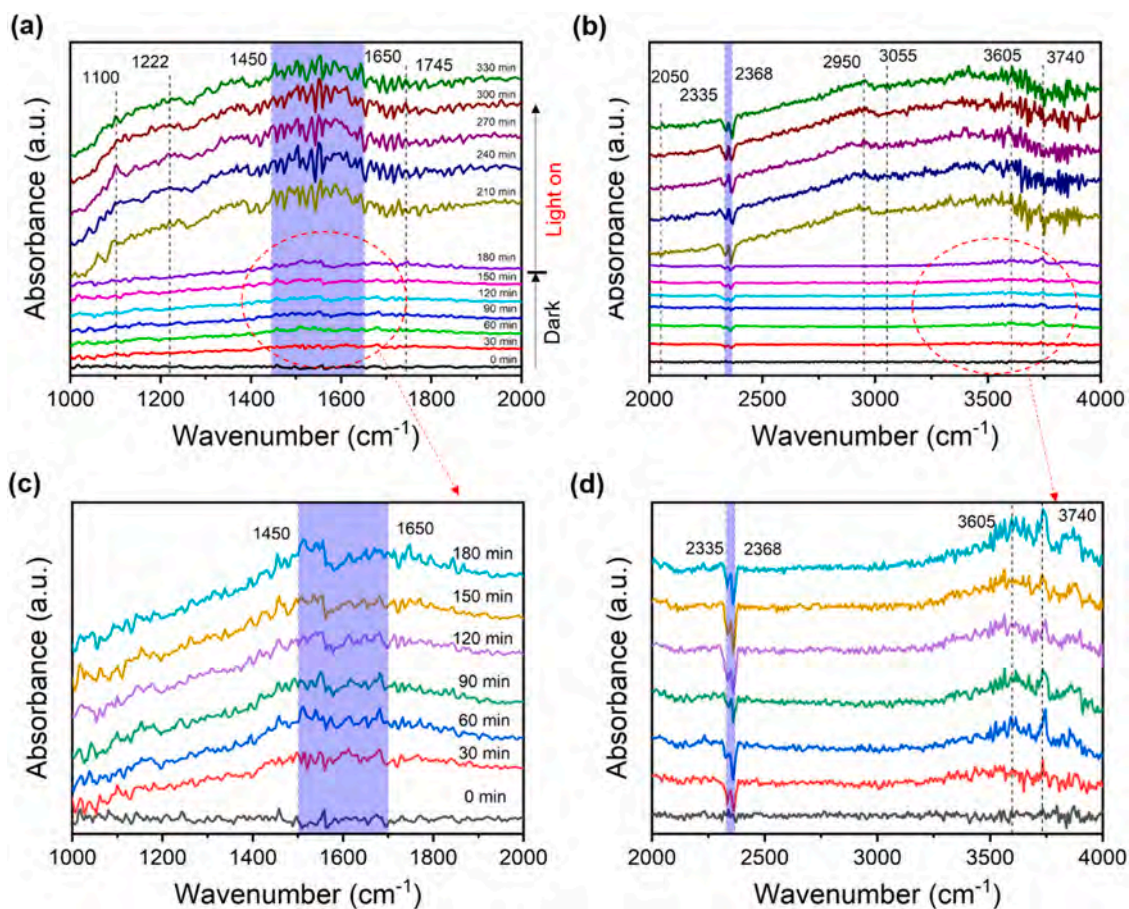
Fig. 8. (a) and (b) The *in-situ* DRIFTS of adsorption and photocatalytic degradation of o-xylene by MOXA-2, (c) and (d) the enlarged *in-situ* DRIFTS of adsorption of o-xylene by MOXA-2.

o-xylene. The peaks at 2950, 3055 cm^{-1} (the vibration of C-H of methyl in toluene) were also observed, indicating the formation of toluene owing to that the photogenerated holes attack the methyl in o-xylene [54,55]. Interesting, almost no peaks for free water (3740 cm^{-1}) was observed after starting the light illumination, while the peak for ν_{O-H} (3605 cm^{-1}) became dominant, indicating that water mainly existed in the form of Fe$_3$-O(OH) with the excitation of light. It was worth noticing that the peak of CO$_2$ increased obviously, confirming that o-xylene molecules were oxidized into CO$_2$, which could then absorb on the surface of MOXA-2. The change of RH in the reaction chamber and the concentration of CO$_2$ in the process of photocatalytic degradation to o-xylene were displayed in Fig. S14a and b. These above results proved that o-xylene molecules were ultimately converted into water and CO$_2$.

Based on the above analysis, the photocatalytic degradation mechanism of BTXS by MOXA-2 was proposed and displayed in Scheme 2. The capture of BTXS molecules would happen due to the adsorption by micropores, the π-π interaction between BTXS molecules and the ligands and the adsorption by Fe$_3$-O clusters. As a strong acidic center, Fe(III) in Fe$_3$-O clusters would get an electron from the adsorbed molecules, which resulted in the consumption of Fe(III) observed in the ESR results. After starting the light irradiation, both components (MIL-100(Fe) xerogel and crystalline MIL-100(Fe) particles) in MOXA-2 could be excited. Electrons were excited into the Fe$_3$-O clusters through the LCCT (ligand-to-cluster charge transfer) mechanism while the holes stayed in the ligands. As a result of band bending at the interface between crystallined MIL-100(Fe) particles and MIL-100(Fe) xerogel, the electrons from the LUMO of MIL-100(Fe) xerogel and the holes from the HOMO of crystallined MIL-100(Fe) particles combined at the interface region, while the electrons in the LUMO of crystallined MIL-100(Fe) particles

and the holes in the HOMO of MIL-100(Fe) xerogel skeleton could be retained. The free electrons would react with O$_2$ to produce strong oxidizing ·O$_2^-$ radicals for the mineralization of BTXS molecules and lead to the oxidization of Fe(II) to Fe(III).

4. Conclusion

The MIL-100 (Fe) MOF/MOX homojunctions with tunable hierarchical pores and homojunction were successful prepared by a one-pot solvothermal method. The tunable hierarchical pores were achieved by adjusting the anions species to control the dissociation rate of metal ions. The MIL-100(Fe) MOF/MOX homojunctions showed high photocatalytic activity towards the degradation of o-xylene and other BTXS (benzene, toluene, p-xylene, m-xylene and styrene). On one hand, benefiting from the hierarchical pores, the diffusion resistance of gaseous BTXS in the pores was reduced, which enabled the effective contact between BTXS molecules and the active sites for PCO reactions. On the other hand, the homojunction between MIL-100(Fe) xerogel and crystalline MIL-100(Fe) particles improved the separation of photogenerated carriers and therefore promote the generation of highly oxidative ·O$_2^-$ radicals. Besides, the conversion between Fe(III) and Fe(II) occurred during the adsorption and photocatalytic degradation of BTXS also benefited the separation of electrons and holes and further improved the photocatalytic reaction activities. The successful preparation of the MIL-100(Fe) MOF/MOX homojunctions provides a new strategy for regulating the formation MOFs with hierarchical pores, and will be an advance in photocatalytic removal of gaseous pollutants.

CRediT authorship contribution statement

Lu Chen: Conceptualization, Investigation, Methodology, Formal analysis, Data curation, Writing – original draft. **Xiao Wang**: Conceptualization, Methodology, Resources, Funding acquisition, Project administration, Validation, Supervision, Writing – review & editing. **Zepeng Rao**: Formal analysis, Investigation, Resources. **Zixia Tang**: Formal analysis, Investigation. **Gansheng Shi**: Formal analysis, Investigation. **Yan Wang**: Formal analysis, Resources. **Guanhong Lu**: Formal analysis, Investigation. **Xiaofeng Xie**: Formal analysis, Project administration. **Deliang Chen**: Formal analysis, Funding acquisition, Resources, Project administration. **Jing Sun**: Investigation, Validation, Funding acquisition, Resources, Project administration.

Declaration of Competing Interest

The authors declare that they have no known competing financial interests or personal relationships that could have appeared to influence the work reported in this paper.

Acknowledgments

Appendix A. Supporting information

Supplementary data associated with this article can be found in the online version at doi:10.1016/j.apcatb.2021.120885.

References

[1] O. Debono, V. Hequet, L. Le Coq, N. Locoge, F. Thevenet, VOC ternary mixture effect on ppb level photocatalytic oxidation: Removal kinetic, reaction intermediates and mineralization, Appl. Catal. B Environ. 218 (2017) 359–369, https://doi.org/10.1016/j.apcatb.2017.06.070.

[2] W. Zhang, G. Li, H. Liu, J. Chen, S. Ma, M. Wen, J. Kong, T. An, Photocatalytic degradation mechanism of gaseous styrene over Au/TiO$_2$@CNTs: Relevance of superficial state with deactivation mechanism, Appl. Catal. B Environ. 272 (2020), 118969, https://doi.org/10.1016/j.apcatb.2020.118969.

[3] D.A. Sarigiannis, S.P. Karakitsios, A. Gotti, I.L. Liakos, A. Katsoyiannis, Exposure to major volatile organic compounds and carbonyls in European indoor environments and associated health risk, Environ. Int. 37 (2011) 743–765, https://doi.org/10.1016/j.envint.2011.01.005.

[4] M. Wen, G. Li, H. Liu, J. Chen, T. An, H. Yamashita, Metal-organic framework-based nanomaterials for adsorption and photocatalytic degradation of gaseous pollutants: recent progress and challenges, Environ. Sci. Nano 6 (2019) 1006–1025, https://doi.org/10.1039/C8EN01167B.

[5] Hong-Cai Zhou, J.R. Long, Omar M. Yaghi, Introduction to Metal-Organic Frameworks, Chem. Rev. 112 (2012) 673–674, https://doi.org/10.1021/cr300014x.

[6] E. Barea, C. Montoro, J.A.R. Navarro, Toxic gas removal-metal-organic frameworks for the capture and degradation of toxic gases and vapours, Chem. Soc. Rev. 43 (2014) 5419–5430, https://doi.org/10.1039/C3CS60475F.

[7] Z. Xue, K. Liu, Q. Liu, Y. Li, M. Li, C.Y. Su, N. Ogiwara, H. Kobayashi, H. Kitagawa, M. Liu, G. Li, Missing-linker metal-organic frameworks for oxygen evolution reaction, Nat. Commun. 10 (2019) 5048, https://doi.org/10.1038/s41467-019-13051.

[8] H. Li, L. Li, R.-B. Lin, W. Zhou, Z. Zhang, S. Xiang, B. Chen, Porous metal-organic frameworks for gas storage and separation: Status and challenges, EnergyChem 1 (2019), 100006, https://doi.org/10.1016/j.enchem.2019.100006.

[9] K. Zhang, X. Xie, H. Li, J. Gao, L. Nie, Y. Pan, J. Xie, D. Tian, W. Liu, Q. Fan, H. Su, L. Huang, W. Huang, Highly Water-Stable Lanthanide-Oxalate MOFs with Remarkable Proton Conductivity and Tunable Luminescence, Adv. Mater. 29 (2017), 1701804, https://doi.org/10.1002/adma.201701804.

[10] X. Meng, B. Gui, D. Yuan, M. Zeller, C. Wang, Mechanized azobenzene-functionalized zirconium metal-organic framework for on-command cargo release, Sci. Adv. 2 (2016), e1600480, https://doi.org/10.1126/sciadv.1600480.

[11] H. Huang, Y. Zhao, Y.M. Bai, F.M. Li, Y. Zhang, Y. Chen, Conductive Metal-Organic Frameworks with Extra Metallic Sites as an Efficient Electrocatalyst for the Hydrogen Evolution Reaction, Adv. Sci. 7 (2020), 2000012, https://doi.org/10.1002/advs.202000012.

[12] L. Chen, X. Wang, Z. Rao, Z. Tang, Y. Wang, G. Shi, G. Lu, X. Xie, D. Chen, J. Sun, In-situ synthesis of Z-scheme MIL-100(Fe)/α-Fe$_2$O$_3$ heterojunction for enhanced adsorption and Visible-light photocatalytic oxidation of O-xylene, Chem. Eng. J. 416 (2021), 129112, https://doi.org/10.1016/j.cej.2021.129112.

[13] P. Li, S. Kim, J. Jin, H.C. Do, J.H. Park, Efficient photodegradation of volatile organic compounds by iron-based metal-organic frameworks with high adsorption capacity, Appl. Catal. B Environ. 263 (2020), 118284, https://doi.org/10.1016/j.apcatb.2019.118284.

[14] S.C. Qi, X.Y. Qian, Q.X. He, K.J. Miao, Y. Jiang, P. Tan, X.Q. Liu, L.B. Sun, Generation of Hierarchical Porosity in Metal-Organic Frameworks by the Modulation of Cation Valence, Angew. Chem. Int. Ed. 58 (2019) 10104–10109, https://doi.org/10.1002/anie.201903323.

[15] Y. Keum, B. Kim, A. Byun, J. Park, Synthesis and Photocatalytic Properties of Titanium-Porphyrinic Aerogels, Angew. Chem. Int. Ed. 59 (2020) 21591–21596, https://doi.org/10.1002/anie.202007193.

[16] R.K. Motkuri, H.V.R. Annapureddy, M. Vijaykumar, H.T. Schaef, P.F. Martin, B.P. McGrail, L.X. Dang, R. Krishna, P.K. Thallapally, Fluorocarbon adsorption in hierarchical porous frameworks, Nat. Commun. 5 (2014) 4368, https://doi.org/10.1038/ncomms5368.

[17] W. Xu, K.B. Thapa, Q. Ju, Z. Fang, W. Huang, Heterogeneous catalysts based on mesoporous metal-organic frameworks, Coord. Chem. Rev. 373 (2018) 199–232, https://doi.org/10.1016/j.ccr.2017.10.014.

[18] H. Deng, S. Grunder, K.E. Cordova, C. Valente, H. Furukawa, M. Hmadeh, F. Gándara, A.C. Whalley, Z. Liu, S. Asahina, H. Kazumori, M. O'Keeffe, O. Terasaki, J.F. Stoddart, O.M. Yaghi, Large-Pore Apertures in a Series of Metal-Organic Frameworks, Science 336 (2012) 1018–1023, https://doi.org/10.1126/science.1220131.

[19] Z. Fang, B. Bueken, D.E. DeVos, R.A. Fischer, Defect-Engineered Metal-Organic Frameworks, Angew. Chem. Int. Ed. 54 (2015) 7234–7254, https://doi.org/10.1002/anie.201411540.

[20] J. Hou, A.F. Sapnik, T.D. Bennett, Metal-organic framework gels and monoliths, Chem. Sci. 11 (2020) 310–323, https://doi.org/10.1039/C9SC04961D.

[21] F. Zhao, W. Yang, Y. Han, X. Luo, W. Tang, T. Yue, Z. Li, A straightforward strategy to synthesize supramolecular amorphous zirconium metal-organic gel for efficient Pb(II) removal, Chem. Eng. J. 407 (2021), 126744, https://doi.org/10.1016/j.cej.2020.126744.

[22] L. Li, S. Xiang, S. Cao, J. Zhang, G. Ouyang, L. Chen, C.Y. Su, A synthetic route to ultralight hierarchically micro/mesoporous Al(III)-carboxylate metal-organic aerogels, Nat. Commun. 4 (2013) 1774, https://doi.org/10.1038/ncomms2757.

[23] P. Horcajada, S. Surble, C. Serre, D.Y. Hong, Y.K. Seo, J.S. Chang, J.M. Greneche, I. Margiolaki, G. Ferey, Synthesis and catalytic properties of MIL-100(Fe), an iron (III) carboxylate with large pores, Chem. Commun. (2007) 2820–2822, https://doi.org/10.1039/B704325B.

[24] H. Wang, P. Rassu, X. Wang, H. Li, X. Wang, X. Wang, X. Feng, A. Yin, P. Li, X. Jin, S.-L. Chen, X. Ma, B. Wang, An Iron-Containing Metal-Organic Framework as a Highly Efficient Catalyst for Ozone Decomposition, Angew. Chem. Int. Ed. 57 (2018) 16416–16420, https://doi.org/10.1002/anie.201810268.

[25] A.P. Grosvenor, B.A. Kobe, M.C. Biesinger, N.S. McIntyre, Investigation of multiplet splitting of Fe 2p XPS spectra and bonding in iron compounds, Surf. Interface Anal. 36 (2004) 1564–1574, https://doi.org/10.1002/sia.1984.

[26] T. Yamashita, P. Hayes, Analysis of XPS spectra of Fe^{2+} and Fe^{3+} ions in oxide materials, Appl. Surf. Sci. 254 (2008) 2441–2449, https://doi.org/10.1016/j.apsusc.2007.09.063.

[27] H. Leclerc, A. Vimont, J.-C. Lavalley, M. Daturi, A.D. Wiersum, P.L. Llwellyn, P. Horcajada, G. Férey, C. Serre, Infrared study of the influence of reducible iron (iii) metal sites on the adsorption of CO, CO$_2$, propane, propene and propyne in the mesoporous metal-organic framework MIL-100, Phys. Chem. Chem. Phys. 13 (2011) 11748–11756, https://doi.org/10.1039/C1CP20502A.

[28] R. Wu, U.A. Jayasooriya, R.D. Cannon, Vibrational coupling in oxo-centred trinuclear clusters: oxygen-16/18 isotopic substitution studies of [Fe$_3$III(O)(O$_2$CC(CH$_3$)$_3$)$_6$(py)$_3$][FeCl$_4$] and [Fe$_2$(III)FeII(O)(O$_2$CC(CH$_3$)$_3$)$_6$(py)$_3$], Spectrochim. Acta A Mol. Biomol. Spectrosc. 56 (2000) 575–579, https://doi.org/10.1016/S1386-1425(99)00156-0.

[29] J.H. Fu, Z. Zhong, D. Xie, Y.J. Guo, D.X. Kong, Z.X. Zhao, Z.X. Zhao, M. Li, SERS-Active MIL-100(Fe) Sensory Array for Ultrasensitive and Multiplex Detection of VOCs, Angew. Chem. Int. Ed. 59 (2020) 20489–20498, https://doi.org/10.1002/anie.202002720.

[30] C. Li, J. Hao, K. Wu, Triethylamine-controlled Cu-BTC frameworks for electrochemical sensing fish freshness, Anal. Chim. Acta 1085 (2019) 68–74, https://doi.org/10.1016/j.aca.2019.07.064.

[31] A. Michota, J. Bukowska, Surface-enhanced Raman scattering (SERS) of 4-mercaptobenzoic acid on silver and gold substrates, J. Raman Spectrosc. 34 (2003) 21–25, https://doi.org/10.1002/jrs.928.

[32] J. Xu, F. Chu, W. Huang, C. Liu, C. Lu, Y. Cui, J. Zhang, X. Liu, Relations of two-photon absorption property and molecular structure in phenylenevinylene chromophores, Proceedings of SPIE 6839 (2008), https://doi.org/10.1117/12.757594.

[33] B. Zhu, G. Liu, L. Chen, L. Qiu, L. Chen, J. Zhang, L. Zhang, M. Barboiu, R. Si, C.-Y. Su, Metal–organic aerogels based on dinuclear rhodium paddle-wheel units: design, synthesis and catalysis, Inorg. Chem. Front. 3 (2016) 702–710, https://doi.org/10.1039/C5QI00272A.

[34] H. Li, M. Eddaoudi, M. O'Keeffe, O.M. Yaghi, Design and synthesis of an exceptionally stable and highly porous metal-organic framework, Nature 402 (1999) 276–279, https://doi.org/10.1038/46248.

[35] W. Lin, X. Xie, X. Wang, Y. Wang, D. Segets, J. Sun, Efficient adsorption and sustainable degradation of gaseous acetaldehyde and o-xylene using rGO-TiO₂ photocatalyst, Chem. Eng. J. 349 (2018) 708–718, https://doi.org/10.1016/j.cej.2018.05.107.

[36] X. Zhang, X. Shi, J. Chen, Y. Yang, G. Lu, The preparation of defective UiO-66 metal organic framework using MOF-5 as structural modifier with high sorption capacity for gaseous toluene, J. Environ. Chem. Eng. 7 (2019) 103405, https://doi.org/10.1016/j.jece.2019.103405.

[37] Z. Wang, A. Mahmood, X. Xie, X. Wang, H. Qiu, J. Sun, Surface adsorption configurations of H₃PO₄ modified TiO₂ and its influence on the photodegradation intermediates of gaseous o-xylene, Chem. Eng. J. 393 (2020), 124723, https://doi.org/10.1016/j.cej.2020.124723.

[38] Z. Gao, J. Wang, Y. Muhammad, Y. Zhang, S.J. Shah, Y. Hu, Z. Chu, Z. Zhao, Z. Zhao, Enhanced moisture-resistance and excellent photocatalytic performance of synchronous N/Zn-decorated MIL-125(Ti) for vaporous acetaldehyde degradation, Chem. Eng. J. 388 (2020), 124389, https://doi.org/10.1016/j.cej.2020.124389.

[39] H. Khajavi, H.A. Stil, H.P.C.E. Kuipers, J. Gascon, F. Kapteijn, Shape and Transition State Selective Hydrogenations Using Egg-Shell Pt-MIL-101(Cr) Catalyst, ACS Catal. 3 (2013) 2617–2626, https://doi.org/10.1021/cs400681s.

[40] Y. Bai, Y. Zhou, J. Zhang, X. Chen, Y. Zhang, J. Liu, J. Wang, F. Wang, C. Chen, C. Li, R. Li, C. Li, Homophase Junction for Promoting Spatial Charge Separation in Photocatalytic Water Splitting, ACS Catal. 9 (2019) 3242–3252, https://doi.org/10.1021/acscatal.8b05050.

[41] F. He, B. Zhu, B. Cheng, J. Yu, W. Ho, W. Macyk, 2D/2D/0D TiO₂/C₃N₄/Ti₃C₂ MXene composite S-scheme photocatalyst with enhanced CO₂ reduction activity, Appl. Catal. B Environ. 272 (2020) 119006, https://doi.org/10.1016/j.apcatb.2020.119006.

[42] F. Xu, K. Meng, B. Cheng, S. Wang, J. Xu, J. Yu, Unique S-scheme heterojunctions in self-assembled TiO₂/CsPbBr₃ hybrids for CO₂ photoreduction, Nat. Commun. 11 (2020) 4613, https://doi.org/10.1038/s41467-020-18350-7.

[43] J. Sun, X. Li, Q. Zhao, J. Ke, D. Zhang, Novel V₂O₅/BiVO₄/TiO₂ Nanocomposites with High Visible-Light-Induced Photocatalytic Activity for the Degradation of Toluene, J. Phys. Chem. C 118 (2014) 10113–10121, https://doi.org/10.1021/jp5013076.

[44] Y. Wu, S. Yuan, R. Feng, Z. Ma, Y. Gao, S. Xing, Comparative study for low-temperature catalytic oxidation of o-xylene over doped OMS-2 catalysts: Role of Ag and Cu, Mol. Catal. 442 (2017) 164–172, https://doi.org/10.1016/j.mcat.2017.09.020.

[45] X. Chen, J.-J. Li, X. Chen, S.-C. Cai, E.-Q. Yu, J. Chen, H. Jia, MOF-Templated Approach for Hollow NiOx/Co₃O₄ Catalysts: Enhanced Light-Driven Thermocatalytic Degradation of Toluene, ACS Appl. Nano Mater. 1 (2018) 2971–2981, https://doi.org/10.1021/acsanm.8b00587.

[46] D. Wang, R. Huang, W. Liu, D. Sun, Z. Li, Fe-Based MOFs for Photocatalytic CO₂ Reduction: Role of Coordination Unsaturated Sites and Dual Excitation Pathways, ACS Catal. 4 (2014) 4254–4260, https://doi.org/10.1021/cs501169t.

[47] D. Wang, M. Wang, Z. Li, Fe-Based Metal-Organic Frameworks for Highly Selective Photocatalytic Benzene Hydroxylation to Phenol, ACS Catal. 5 (2015) 6852–6857, https://doi.org/10.1021/acscatal.5b01949.

[48] E.D. Bloch, L.J. Murray, W.L. Queen, S. Chavan, S.N. Maximoff, J.P. Bigi, R. Krishna, V.K. Peterson, F. Grandjean, G.J. Long, B. Smit, S. Bordiga, C.M. Brown, J.R. Long, Selective Binding of O₂ over N₂ in a Redox-Active Metal-Organic Framework with Open Iron(II) Coordination Sites, J. Am. Chem. Soc. 133 (2011) 14814–14822, https://doi.org/10.1021/ja205976v.

[49] Z. Lu, J. Liu, X. Zhang, Y. Liao, R. Wang, K. Zhang, J. Lyu, O.K. Farha, J.T. Hupp, Node-Accessible Zirconium MOFs, J. Am. Chem. Soc. 142 (2020) 21110–21121, https://doi.org/10.1021/jacs.0c09782.

[50] M.D. Hernández-Alonso, I. Tejedor-Tejedor, J.M. Coronado, M.A. Anderson, Operando FTIR study of the photocatalytic oxidation of methylcyclohexane and toluene in air over TiO₂-ZrO₂ thin films: Influence of the aromaticity of the target molecule on deactivation, Appl. Catal. B Environ. 101 (2011) 283–293, https://doi.org/10.1016/j.apcatb.2010.09.029.

[51] J. Li, Xa Dong, G. Zhang, W. Cui, W. Cen, Z. Wu, S.C. Lee, F. Dong, Probing ring-opening pathways for efficient photocatalytic toluene decomposition, J. Mater. Chem. A 7 (2019) 3366–3374, https://doi.org/10.1039/C8TA11627J.

[52] Y. Wu, S. Shi, S. Yuan, T. Bai, S. Xing, Insight into the enhanced activity of Ag/NiOx-MnO₂ for catalytic oxidation of o-xylene at low temperatures, Appl. Surf. Sci. 479 (2019) 1262–1269, https://doi.org/10.1016/j.apsusc.2019.01.134.

[53] Z. Rao, G. Lu, A. Mahmood, G. Shi, X. Xie, J. Sun, Deactivation and activation mechanism of TiO₂ and rGO/Er³⁺-TiO₂ during flowing gaseous VOCs photodegradation, Appl. Catal. B Environ. 284 (2021) 119813, https://doi.org/10.1016/j.apcatb.2020.119813.

[54] R. Mi, D. Li, Z. Hu, R.T. Yang, Morphology Effects of CeO₂ Nanomaterials on the Catalytic Combustion of Toluene: a Combined Kinetics and Diffuse Reflectance Infrared Fourier Transform Spectroscopy Study, ACS Catal. 11 (2021) 7876–7889, https://doi.org/10.1021/acscatal.1c01981.

[55] J. Wang, J. Li, W. Yang, Y. Liu, H. Wang, Q. Geng, F. Dong, Promote reactants activation and key intermediates formation for facilitated toluene photodecomposition via Ba active sites construction, Appl. Catal. B Environ. 297 (2021), 120489, https://doi.org/10.1016/j.apcatb.2021.120489.